Petroleum Science 23 (2026) 4621–4633

Contents lists available at ScienceDirect

Petroleum Science

journal homepage: www.keaipublishing.com/en/journals/petroleum-science

Original Paper

Depth-domain inversion with angle-domain point-spread function for quantitative reservoir characterization: A case study from the Northern Viking Graben, North Sea

Lei Zhao [a,b,c], Wei-Jian Mao [a,b,*], Xue Li [d]

[a] *Center for Computational and Exploration Geophysics, Innovation Academy for Precision Measurement Science and Technology, Chinese Academy of Sciences, Wuhan, 430077, Hubei, China*
[b] *State Key Laboratory of Precision Geodesy, Wuhan, 430077, Hubei, China*
[c] *University of Chinese Academy of Sciences, Beijing, 100049, China*
[d] *Exploration and Development Research Institute of HuaBei Oilfield Company, Cangzhou, 062552, Hebei, China*

A R T I C L E I N F O

Article history:
Received 17 November 2025
Received in revised form
26 January 2026
Accepted 17 March 2026
Available online 23 March 2026

Edited by Meng-Jiao Zhou

Keywords:
Depth-domain inversion
Point-spread function (PSF)
Elastic parameter inversion
Reservoir characterization
Northern Viking Graben
North Sea Basin

A B S T R A C T

Amplitude-preserving depth-domain prestack inversion using the point-spread function (PSF) has emerged as a powerful approach for quantitative reservoir characterization. This technique employs the PSF to approximate the Hessian operator, illumination-induced blurring is compensated during imaging, thereby improving amplitude fidelity and spatial resolution. However, most existing depth-domain inversion studies have focused on poststack applications. Systematic investigations of prestack inversion—particularly for quantitative fluid characterization—remain limited. To address this limitation, we develop a depth-domain prestack inversion framework that leverages an angle-domain Gaussian-beam PSF. Under high-frequency asymptotic assumptions, we derive an analytical expression for the angle-domain Gaussian-beam PSF and compute PP-wave PSFs to approximate the local Hessian, which we incorporate directly into the inversion operator as a local-Hessian preconditioner. The framework combines a nonstationary convolution model with the Aki–Richards approximation to simultaneously invert for elastic parameters in the depth domain. Applied to a 2D marine streamer line from the Northern Viking Graben in the North Sea, the method reveals multiple low-V_p/V_s anomalies within Paleocene and Jurassic sandstones that correspond to hydrocarbon-bearing intervals identified from well data. A depth-domain ϕ_w (water-filled porosity) section is then constructed through a well-log-calibrated V_p/V_s–ϕ_w relationship established for this study area, which effectively discriminates potential hydrocarbon reservoirs. These results demonstrate that the angle-domain PSF–based depthdomain prestack inversion exhibits robust applicability and geological consistency in structurally complex rift basins, providing a novel pathway for quantitative depth-domain reservoir characterization.

1. Introduction

Conventional seismic inversion workflows are primarily based on the time-domain wavelet convolution model, commonly referred to as prestack amplitude variation with offset (AVO) or amplitude variation with angle (AVA) inversion (Hilterman, 1990; Buland and Omre, 2003), which employs time-domain angle gathers to estimate lithologic and fluid-sensitive parameters (Wang et al., 2022). Because of its effectiveness in attribute characterization and fluid prediction, this approach has been extensively applied in both academic and industrial practice (Zong et al., 2021; Kumar, 2023; Zuo et al., 2025). However, both the inversion process and the inverted parameter models are defined in the time domain (Wang et al., 2022). In practical applications, multiple time-to-depth conversions are required to integrate inversion results with well logs and other depth-domain datasets. This procedure is not only complex but also highly susceptible to error propagation, ultimately compromising the accuracy of reservoir characterization. These issues are particularly severe in rift basins, where strong lateral velocity variations, dense fault systems, and

* Corresponding author.
E-mail address: wjmao@whigg.ac.cn (W.-J. Mao).
Peer review under the responsibility of China University of Petroleum (Beijing).

https://doi.org/10.1016/j.petsci.2026.03.038
1995-8226/

Table 1
Acquisition parameters of the North Viking Graben seismic survey.

Parameter	Value
Type of energy source	Bolt air guns
Number of shot points	1001
Number of receivers per shot	120
Receiver spacing	25 m
Record length sampling interval	6 s
Sampling interval	4 ms
Near offset to far offset	262–3237 m

rapid facies transitions which can markedly amplify time–depth conversion errors and amplitude distortions, as exemplified by the North Viking Graben in the North Sea (Madiba and McMechan, 2003; Zachariah et al., 2009). Consequently, the uncertainty associated with conventional time-domain prestack inversion increases substantially, underscoring the need to perform inversion directly within a unified depth-domain framework to overcome these inherent limitations.

Depth-domain prestack inversion enables accurate registration of seismic data with geological structures, thereby eliminating the need for time–depth conversions. However, a major technical challenge in such inversion lies in estimating the depth-domain wavelet (Zhang and Fomel, 2017; Wei et al., 2017). Because seismic data are inherently nonstationary, the stationary-wavelet assumption commonly used in the time domain is not directly applicable (An et al., 2025). Accordingly, several one-dimensional depth-domain methods based on nonstationary convolution have been proposed. For example, in some carbonate reservoirs, integrated analysis of seismic and well data can be used to estimate layer-constant velocities, thereby facilitating depth-domain wavelet extraction and enabling one-dimensional nonstationary convolution (Singh, 2012). Alternatively, depth–wavenumber decomposition can be employed to derive depth-varying wavelets (Zhang and Deng, 2023). Grana (2016) combined the nonstationary convolution model with a Bayesian linear optimization framework, integrating physical modeling with statistical learning, and achieved fast depth-domain inversion via explicit analytical expressions (Lang and Grana, 2017; Sengupta et al., 2021). However, because these methods rely on one-dimensional assumptions, they cannot adequately account for multidimensional effects and amplitude distortions introduced by complex geological structures and spatially varying acquisition geometries, thereby limiting their practical applicability.

In recent years, amplitude-preserving inversion in the image (depth) domain, which leverages the point-spread function (PSF), has attracted considerable attention. The PSF provides a comprehensive characterization of wavefield distortions introduced by the migration operator, acquisition aperture, and velocity field, enabling direct inversion on prestack depth-migrated images without the need for explicit wavelet estimation (Schuster and Hu, 2000; Fletcher et al., 2012). By approximating the local Hessian, PSF-based formulations can correct illumination-related amplitude distortions caused by complex structures and irregular acquisition coverage (Fletcher et al., 2016; Duan et al., 2023). The computation of the PSF is inherently linked to the underlying migration engine—whether wave-equation-based or ray-based—since each framework imposes a different balance between computational efficiency and modeling accuracy (Hill, 2001; Sherwood et al., 2009; Gelius et al., 2002; Lecomte, 2008; Yue et al., 2021; Jiang et al., 2022; Shi et al., 2023). Moreover, PSF-based methods have evolved from high-resolution reservoir modeling, image-domain deconvolution, and poststack impedance inversion to more general image-domain least-squares migration (IDLSM) and angle-domain PSF-based prestack inversion, thereby improving imaging resolution and amplitude fidelity (Lecomte et al., 2015; Letki et al., 2015; Fletcher et al., 2016; Dai et al., 2019; Osorio et al., 2021; Mao et al., 2022; Yang et al., 2022; Duan et al., 2023; Zhang et al., 2024a). Most of these developments have been implemented in the poststack inversion, whereas only in recent years have PSF applications been extended toward prestack inversion.

Several representative studies exemplify these recent advances. For instance, Valenciano et al. (2019) proposed an angle-domain PSF-based least-squares wave-equation migration approach. Zhang et al. (2024b) developed an angle-dependent IDLSM method based on full-wave Green's functions, incorporating regularization to stabilize the inversion and improve the estimation of reflection coefficients. In parallel, Cavalca and Fletcher (2023) established a true-amplitude AVA inversion framework in the depth domain, based on Kirchhoff migration, to directly estimate elastic parameters. Although these PSF-based prestack inversion studies have improved amplitude fidelity and parameter estimation, their applications are largely restricted to structurally simple settings with well-defined horizons, and often remain focused on high-precision reflectivity inversion (Bai and Yilmaz, 2022; Zhang et al., 2024b). For faulted and rifted basins characterized by complex geological structures, achieving stable and simultaneous depth-domain prestack multi-parameter inversion for direct application to quantitative reservoir characterization and fluid identification remains challenging (Cavalca and Fletcher, 2023).

To overcome these limitations, we propose a depth-domain prestack inversion method that incorporates angle-domain Gaussian-beam PSFs. This work constitutes, to our knowledge, the first systematic application of an angle-domain PSF–based depth-domain prestack inversion to a structurally complex rift basin, with the objective of directly and quantitatively estimating reservoir elastic parameters and fluid properties. Specifically, high-fidelity elastic parameters are first derived through simultaneous inversion. Subsequently, a rock-physics mapping between well-log elastic parameters V_p/V_s and water-filled porosity (ϕ_w) is established and applied to the inverted parameters to obtain a depth-domain ϕ_w section, thereby enabling quantitative interpretation of fluid content and enhancing the interpretability of the V_p/V_s ratio (Madiba and McMechan, 2003; Zhou et al., 2023). The Paleocene and Jurassic reservoirs in the North Viking Graben are selected as the target area to validate the feasibility of the proposed method under geologically complex conditions. Comprehensive well-log and rock-physics data from the study area provide strong constraints on the inversion process and enable robust independent validation of the results. The field application demonstrates that the inverted parameters are highly consistent with well-log–derived fluid indicators, clearly delineating potential hydrocarbon reservoir zones within the Paleocene and Jurassic formations. In summary, this study presents an innovative depth-domain prestack inversion framework that demonstrates strong potential for quantitative reservoir characterization and fluid identification in structurally complex rift basins.

2. Regional setting

The North Viking Graben is situated in the northern part of the North Sea Basin, approximately between 59° and 61°N. It is bounded to the east and west by the Horda Platform and the East Shetland Platform, respectively; to the south it merges into the South Viking Graben, and to the north it transitions toward the Norwegian Sea (Fig. 1). The basin experienced two main extensional phases during the Late Permian–Early Triassic and the

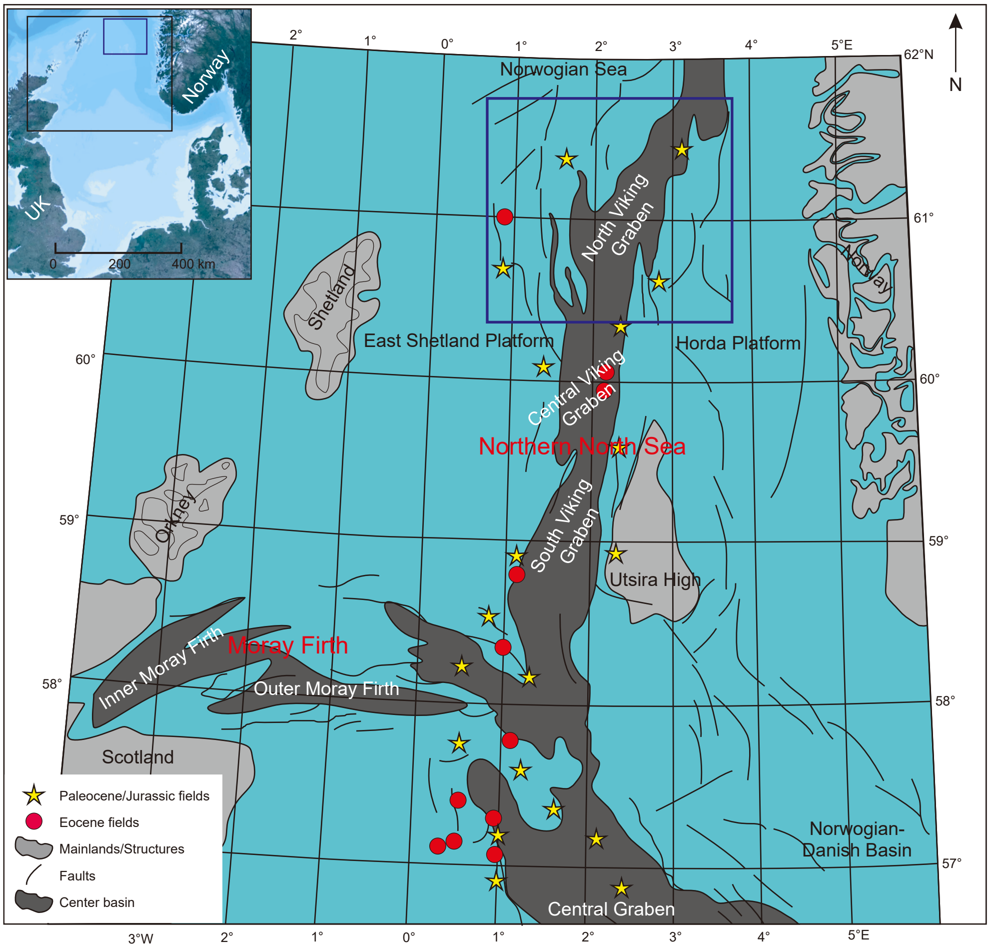

Fig. 1. Structural framework of the North Sea Basin showing major structural elements, platforms/highs, and faults, with surrounding landmasses indicated. Yellow stars mark Paleocene and Jurassic oil fields, whereas red circles denote Eocene fields. The North Sea and the study area are outlined in black and blue, respectively (modified from Surlyk et al., 2003).

Middle Jurassic–Early Cretaceous periods (Underhill and Richardson, 2022). These extensional episodes produced systems of en echelon grabens and half-grabens and rotated fault blocks that not only controlled the distribution of syn-rift depositional systems but also influenced the infill architecture of the post-rift sequences (Madiba and McMechan, 2003). The stratigraphic framework of the area is shown in Fig. 2. A key tectono-stratigraphic boundary is represented by the Base Cretaceous Unconformity (BCU), which separates the underlying Jurassic syn-rift succession from the overlying Cretaceous–Cenozoic post-rift sequences (Fig. 3).

Jurassic reservoirs constitute the principal exploration targets in the North Viking Graben and occur predominantly beneath the BCU. Trap formation in the area was primarily controlled by intense faulting, manifested as fault-bounded closures and, locally, as stratigraphic truncations against the BCU (Turner et al., 2018). During the Jurassic, a substantial influx of coarse clastics generated high-quality reservoirs—most notably within the Brent Group—in environments ranging from fluvial and deltaic to shallow marine settings (Underhill and Richardson, 2022). These sand bodies commonly stack vertically and are separated by deeper-water shales (e.g., the Heather and Draupne formations of the Viking Group), together forming effective reservoir–seal pairs (Zhao et al., 2023). Among these, the Draupne Formation—a regionally extensive, organic-rich marine shale—represents the principal source rock in the area (Gautier, 2005). Consequently, prolific reservoirs commonly develop near the crests of tilted fault blocks and other local structural highs.

Paleogene reservoirs constitute another major exploration target. During the Paleocene, the basin entered a post-rift stage characterized by markedly reduced tectonic activity, and sedimentation became dominated by slope fans and turbidite sands that prograded basinward along the basin margins (Zachariah et al., 2009). Consequently, trap styles shifted toward lithologic types, typically associated with pinchouts and lenticular sand bodies. On seismic sections, the Paleocene interval (labeled PA) commonly exhibits prominent anomalous reflections interpreted as widespread turbidites or mass-transport deposits, which can readily develop into effective lithologic traps (Fig. 3).

3. Data and method

This section describes the seismic and well-log data used in this study and outlines the workflow of the angle-domain PSF–based depth-domain inversion.

3.1. Data

The seismic dataset was acquired using a marine streamer survey comprising 1001 shot points acquired along an east–west-oriented line. Each shot was recorded by 120 receivers spaced 25 m apart and a temporal sampling interval of 4 ms, yielding near and

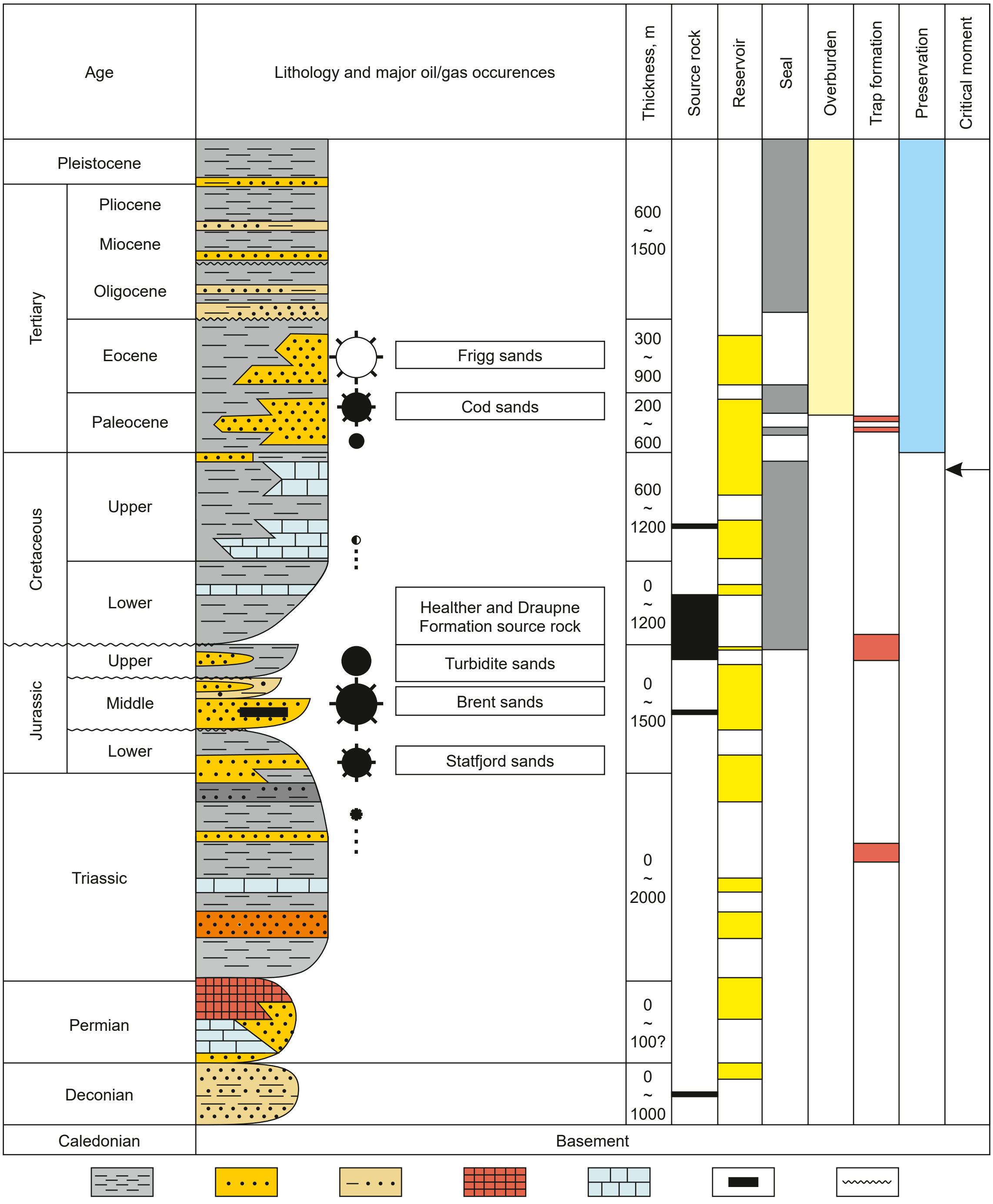

Fig. 2. Stratigraphic column of the North Sea showing source–reservoir–seal assemblages and key petroleum system events.

far offsets of 262 m and 3237 m, respectively. The main acquisition parameters of the North Viking Graben seismic survey are summarized in Table 1. Two wells lie within the study area, and their relative positions are shown in Fig. 3. In addition to the primary elastic logs, the dataset includes log-derived rock-physics attributes (Lee and Collett, 2001), including volumetric fractions of key minerals (illite, calcite, and quartz) and pore fluids (gas, oil, and water). To provide an explicit well-based reference for the subsequent crossplot analysis and fluid calibration, we present a localized rock-physics log panel from Well A, showing the vertical variations of these mineral and fluid fractions (Fig. 4).

3.2. Depth-domain inversion and objective function

In IDLSM, the prestack depth-migrated image $\mathbf{R}_{\mathrm{mig}}$ is considered the outcome of applying a blurring operator $\mathbf{H}$ to the true reflectivity model $\mathbf{R}_{\mathrm{t}}(\mathbf{y}, \theta)$ (Zhang et al., 2024b), as given by

$$\mathbf{R}_{\mathrm{mig}}(\mathbf{x}, \theta) = \int \mathrm{d}\mathbf{y} \int \mathrm{d}\theta_{\mathrm{t}} \mathbf{H}(\mathbf{x}, \theta; \mathbf{y}, \theta_{\mathrm{t}}) \mathbf{R}_{\mathrm{t}}(\mathbf{y}, \theta_{\mathrm{t}}), \tag{1}$$

where $\mathbf{R}_{\mathrm{mig}}(\mathbf{x}, \theta)$ denotes the multicomponent angle-domain common-image gathers (ADCIGs), and θ represents the index of

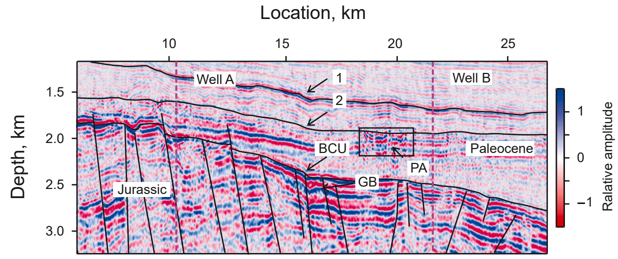

Fig. 3. Interpreted seismic section across the Northern Viking Graben showing the Cretaceous unconformity (BCU), the Paleocene amplitude anomaly (PA), and the tilted Jurassic graben blocks (GB). Horizons 1, 2, and the BCU were used for interwell interpolation during the inversion.

the angle direction of the ADCIGs. $\mathbf{R}_t(\mathbf{y}, \theta_t)$ represents the true plane-wave reflection coefficient of the subsurface reflector at position $\mathbf{y}$, while θ_t is the corresponding reflection angle independent of source–receiver geometry. The blurring operator $\mathbf{H} = \mathbf{L}^\top\mathbf{L}$ represents the Gaussian-beam angle-domain Hessian operator, which encapsulates the combined effects of the elastic Gaussian-beam forward operator $\mathbf{L}$ and its adjoint (migration) operator $\mathbf{L}^\top$. Physically, $\mathbf{H}$ can be regarded as a measure of illumination variations associated with wavefield propagation (velocity heterogeneity) and acquisition constraints (survey geometry, aperture limitation, and band-limited source wavelet). Appendix A provides the detailed analytical derivation of the angle-domain Hessian operator.

The full Hessian is the four-dimensional operator $\mathbf{H}(\mathbf{x}, \theta; \mathbf{y}, \theta_t)$. Constructing the complete operator is therefore computationally prohibitive. A practical remedy is to approximate the Hessian matrix with the PSF. Following a perturbation argument, let $\delta\mathbf{x}$ be a small spatial displacement about $\mathbf{x}$ and define the neighboring point $\mathbf{y} = \mathbf{x} + \delta\mathbf{x}$. With this notation, the image-domain forward problem in Eq. (1) can be rewritten as

$$\mathbf{R}_{\mathrm{mig}}(\mathbf{x}, \theta) = \int \mathrm{d}\mathbf{y}\mathbf{PSF}(\mathbf{x}, \theta; \mathbf{y})\mathbf{R}_t(\mathbf{y}, \theta), \tag{2}$$

with

$$\begin{aligned}\mathbf{PSF}(\mathbf{x}, \theta; \mathbf{y}) &= \iint \mathrm{d}\mathbf{x}_r\, \mathrm{d}\mathbf{x}_s \int \mathrm{d}\omega\, \omega^4 |F(\omega)|^2\, \delta(\theta - \theta_{\mathbf{x}}) \\ &\times \mathbf{W}^\top(\mathbf{x}_r)\, \mathbf{G}^*(\mathbf{x}, \mathbf{x}_r, \omega)\, \mathbf{W}(\mathbf{x}_r)\, \mathbf{G}^*(\mathbf{x}, \mathbf{x}_s, \omega) \\ &\times \mathbf{Q}^\top(\theta_{\mathbf{x}}, \omega)\mathbf{Q}(\theta_{\mathbf{y}}, \omega)\mathbf{G}(\mathbf{y}, \mathbf{x}_r, \omega)\, \mathbf{G}(\mathbf{y}, \mathbf{x}_s, \omega),\end{aligned} \tag{3}$$

where $\mathbf{PSF}(\mathbf{x}, \theta; \mathbf{y})$ denotes the high-frequency asymptotic Gaussian-beam angle-domain PSFs. $F(\omega)$ denotes the source wavelet. In the source–receiver integral, $\delta(\theta - \theta_{\mathbf{x}})$ is interpreted as a mapping function that selects specific half-scattering angles. $\mathbf{Q}$ is the linear scaling factor that relates the plane-wave reflection coefficient to the scattering-potential function, with different reflection modes corresponding to different scaling factors. The superscript * denotes the complex conjugate. $\mathbf{W}(\mathbf{x}_r)$ denotes a 3×3 transformation matrix used to convert the data at the receiver location from the ray-centered to the Cartesian coordinate system (Červený, 2000; Li and Mao, 2016). $\mathbf{G}(\mathbf{x}, \mathbf{x}_i, \omega)$ denotes the 3×3 elastic Green's tensor, expressed in Gaussian-beam form, that describes wave propagation from $\mathbf{x}_i$ to $\mathbf{x}$, where $\mathbf{x}_i$ corresponds to either the source location $\mathbf{x}_s$ or the receiver location $\mathbf{x}_r$. The subscripts in $\theta_{\mathbf{x}}$ and $\theta_{\mathbf{y}}$ emphasize the dependence of the half-scattering angle on the spatial positions $\mathbf{x}$ and $\mathbf{y}$, respectively. Appendix B provides the derivations of Eqs. (2) and (3) and discusses the high-frequency asymptotic conditions.

Fig. 5 presents the Gaussian-beam angle-domain PSFs of the two-dimensional streamer dataset from the Viking Graben, computed according to Eq. (3). Fig. 6(a) and (b) show localized sections of the extracted angle-domain PSFs at 15° and 30°, respectively. The angle-domain PSFs exhibit significant spatial and angular variations across the study area. These variations directly reflect changes in the local Hessian operator at the scatterer positions and represent localized seismic imaging responses. Consequently, PSFs can be regarded as spatially varying two- or three-dimensional seismic wavelets in the depth domain, providing both vertical and lateral resolution in contrast to conventional one-dimensional wavelets. In practical applications, it is not necessary to compute PSFs at every imaging point. To reduce memory requirements and computational cost, PSFs are typically calculated within a local spatial window centered on a representative point, while those at neighboring locations are obtained through spatial linear interpolation (Mao et al., 2022; Duan et al., 2023).

Furthermore, a representative location was selected to compare the PSFs at incidence angles of 15°, 25°, 35°, and 45°, as illustrated in Fig. 7. The first row displays the central traces of the PSFs, and the second row shows their corresponding wavenumber spectra. The results show that, as the incidence angle increases, the horizontal wavenumber spectrum first broadens and then narrows, while the maximum frequency decreases progressively. These observations clearly demonstrate the strong angle dependence of angle-domain PSFs in the spatial–frequency domain (Jensen et al., 2021).

We define a three-dimensional Earth model $\mathbf{m}$ characterized by its elastic properties, including the ratio of V_p to V_s and the density. The corresponding plane-wave reflectivity is denoted by $\mathbf{R}(\mathbf{m})$. In this study, the reflectivity operator is formulated using the Aki–Richards approximation (Aki and Richards, 1980). To obtain the optimal model, the simulated nonstationary convolution

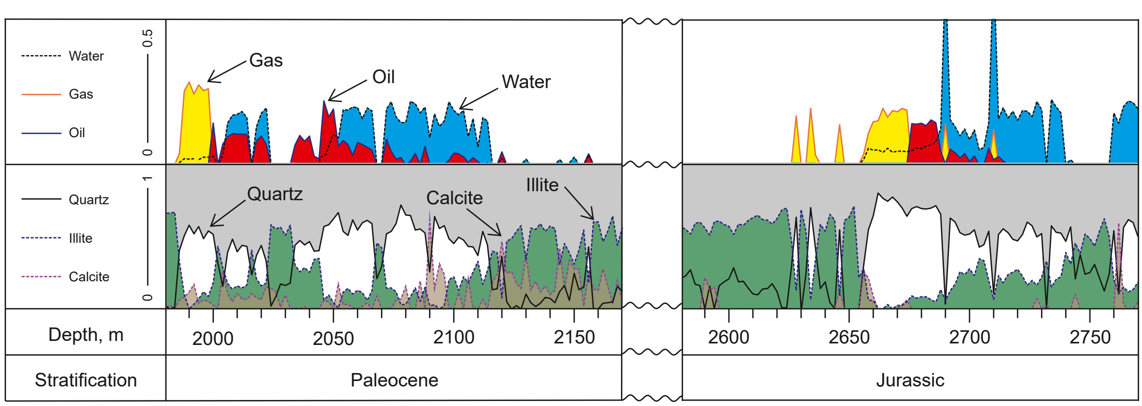

Fig. 4. Vertical distributions of mineral compositions and fluid volume fractions from Well A over the interval of interest.

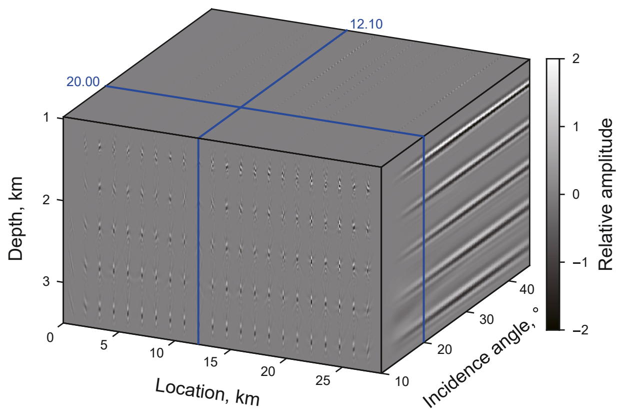

Fig. 5. A part of angle-domain PSFs of the North Viking Graben.

process in Eq. (2) is matched to the migrated image $\mathbf{R}_{\mathrm{mig}}$, and the model is iteratively updated until the best-fitting result is achieved. The objective function to be minimized is thus defined as

$$f(\mathbf{m}) = \frac{1}{2\eta^2}\left\|\mathbf{PSF}*\mathbf{R}(\mathbf{m}) - \mathbf{R}_{\mathrm{mig}}\right\|^2 + \chi\sum_{i,k}\varphi\left(g_{i,k}*\mathbf{R}(\mathbf{m})\right) + \gamma\sum_{i,k}\varphi\left[g_{i,k}*(\mathbf{R}(\mathbf{m}) - \mathbf{R}(\mathbf{m_0}))\right], \quad (4)$$

where $\mathbf{R}\ (\mathbf{m}_0)$ denotes the prior model. $\|\cdot\|$ represents the Euclidean norm, η^2 is the variance of the Gaussian distribution, and $g_{i,k}$ denotes the prior regularization filters configured as first- and second-order derivative operators; subscript i and k represent the kth filter centered on the ith image point. In the following experiments, the derivative filters are defined as $[-1,1]$, $[-1,1]^\top$, $[-1,2,-1]$, $[-1,2,-1]^\top$, and $[-1,\ 1;\ 1,-1]$. The symbol $*$ denotes the convolution operator, while χ and γ are scaling factors controlling the relative weights of the corresponding terms. $\varphi(\mathbf{z}) = |\mathbf{z}|^\ell$ represents the sparse regularization function (Levin et al., 2007), where the norm parameter ℓ controls the sparsity level of the reconstructed model.

Eq. (4) incorporates regularization, where prior knowledge acts as a guiding term that directs the parameter estimation and mitigates the ill-posed nature of the inversion problem. When $\varphi(\mathbf{z}) = |\mathbf{z}|^2$, the prior model follows a Gaussian distribution. By taking the derivative of $\mathbf{R}$ in Eq. (4) and setting it to zero, the problem can be transformed into a linear system. Optimization problems involving Gaussian priors are convex, which allows closed-form analytical solutions. In contrast, the derivatives of prior images are often sparse rather than Gaussian distributed. Therefore, we set the sparse regularization function $\varphi(\mathbf{z}) = |\mathbf{z}|^{0.8}$, which makes $\varphi(\mathbf{z})$ a nonconvex function. The corresponding objective function is solved using the iterative reweighted least-squares algorithm (Duan et al., 2023).

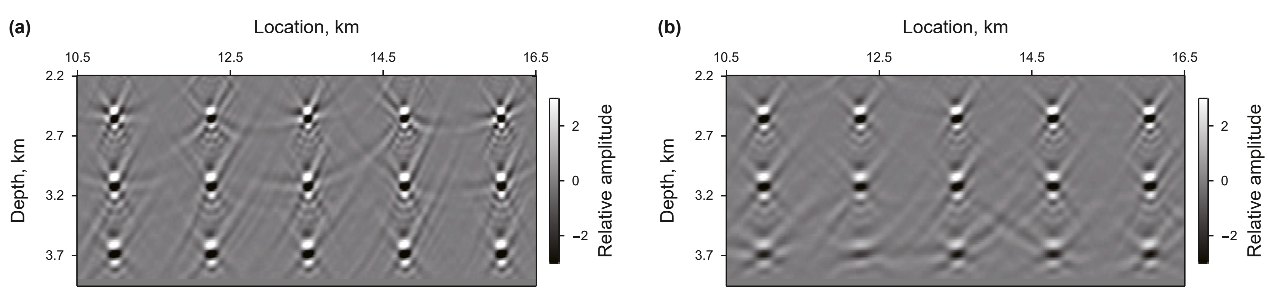

Fig. 6. **(a)** A part of angle-domain PSFs for PP wave PSFs at the angle of 15° and **(b)** PP wave PSFs at the angle of 30°.

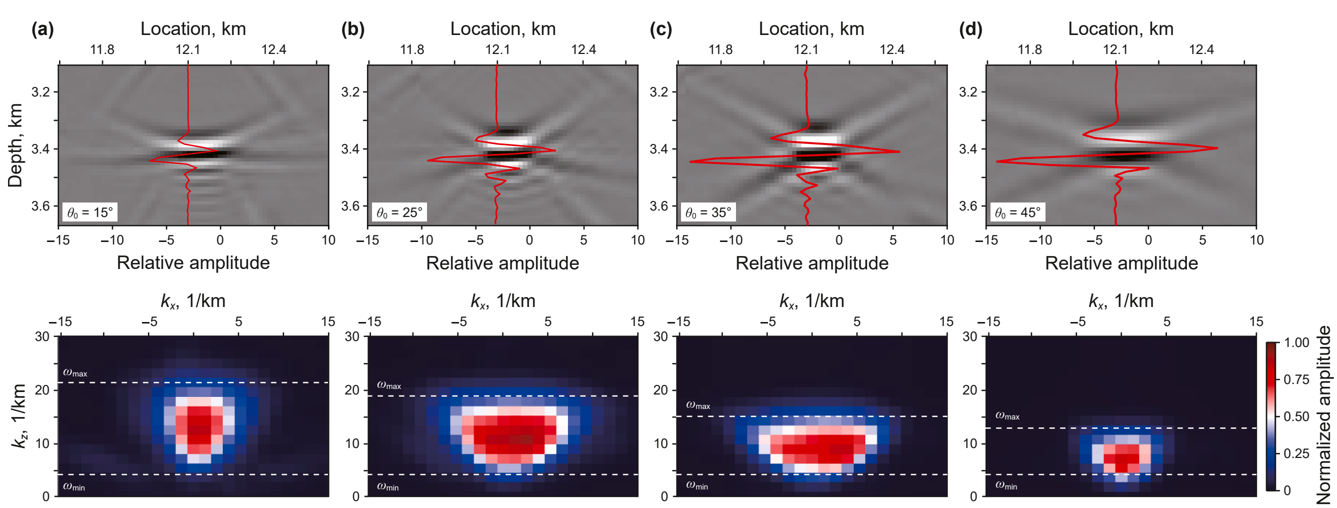

Fig. 7. Comparison of angle-dependent PSFs at a fixed spatial location, showing (top) spatial distributions with overlaid central-trace profiles and (bottom) wavenumber spectra for incidence angles of 15°, 25°, 35°, and 45°.

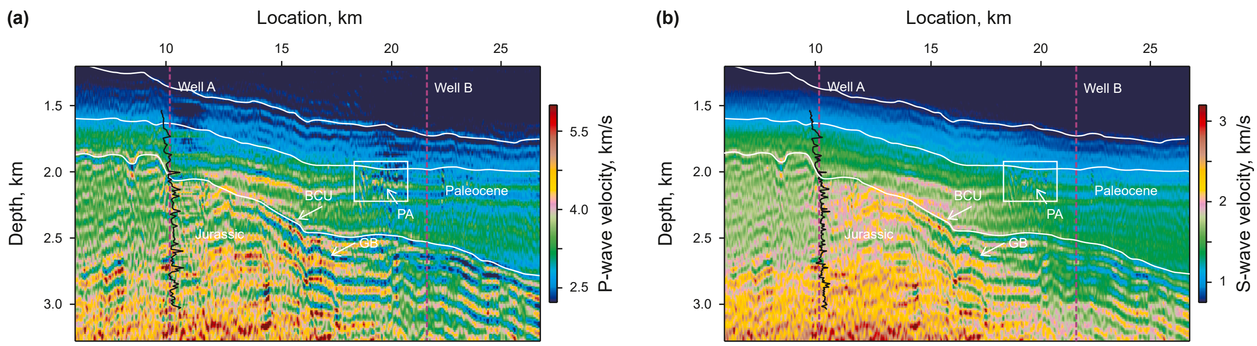

Fig. 8. Inverted profiles of elastic parameters. **(a)** P-wave velocity and **(b)** S-wave velocity. The black curves denote the well logs.

4. Results

This section presents the main results of the angle-domain PSF–based depth-domain inversion. It first presents the inverted elastic parameters, then analyzes the lithology and fluid sensitivity of the V_p/V_s ratio, and finally establishes a V_p/V_s–ϕ_w relationship for quantitative fluid interpretation in the depth domain.

4.1. Depth-domain elastic inversion results

Before performing the depth-domain inversion, the geological background model was constructed by integrating the seismic velocity field with well-log data to generate the required low-frequency prior. The objective function Eq. (4), formulated within the nonstationary convolution framework Eq. (2), was then used to simultaneously invert for V_p, V_s, and density (not shown) by fitting the angle-dependent reflectivity to the multi-angle prestack data. Fig. 8(a) and (b) present the inverted depth-domain profiles of P-wave and S-wave velocities, respectively. The results exhibit pronounced lateral variations in both V_p and V_s within the reservoir interval, particularly in the strata beneath the BCU. Major stratigraphic boundaries and lateral heterogeneities are clearly delineated, and the inverted velocity profiles show strong agreement with the corresponding well-log curves, confirming the robustness and reliability of the inversion results. It should be emphasized that a single elastic parameter is insufficient for unambiguous identification of pore-fluid types, as the velocity ranges associated with oil-, gas-, and water-bearing formations commonly overlap under varying lithological and porosity conditions (Lee and Collett, 2001; Yuan et al., 2022; Wang et al., 2024). Therefore, in the subsequent analysis, fluid-sensitive parameters such as the P- to S-wave velocity ratio, combined with rock-physics constraints, are introduced to enhance the reliability of fluid discrimination.

4.2. V_p/V_s characteristics

In reservoir characterization and fluid prediction, the P- to S-wave velocity ratio (V_p/V_s) is highly sensitive to pore-fluid properties, as it reflects the combined influence of rock-frame stiffness and the compressibility of the pore fluids (Wu et al., 2023). Previous studies have demonstrated that gas-bearing sandstones typically exhibit anomalously low V_p/V_s ratios, whereas water sandstones, siltstones, and shales generally follow the background trend (Ostrander, 1984; Qin et al., 2022; Olutoki et al., 2024). A comparable trend is also observed later in this study. The V_p/V_s ratio section, derived from the inverted V_p and V_s profiles (Fig. 9), reveals several low-V_p/V_s anomalies within the Jurassic reservoir interval that are not distinctly observable in the individual velocity sections. However, a low V_p/V_s anomaly alone does not necessarily indicate the presence of gas; lithological and fluid effects must be further discriminated through rock-physics analysis. In this study, the water-filled porosity ϕ_w is selected as the fluid-indicator parameter. Using well-log data as constraints, an empirical relationship between the V_p/V_s ratio and ϕ_w is established from the crossplot of these two parameters, which is then used for quantitative mapping and interpretation. Here, ϕ_w is defined as the sum of the volumetric fractions of movable water, bound water, and isolated (disconnected) water within the pore space.

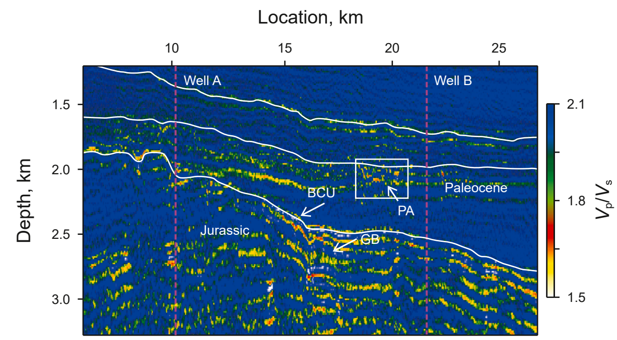

Fig. 9. Inverted V_p/V_s ratio section.

4.3. V_p/V_s–ϕ_w crossplot, well calibration, and ϕ_w mapping

Prior to constructing the crossplot, all well-log curves were depth-matched and resampled to a consistent vertical resolution, and anomalous log values were screened and removed. Within the depth interval of interest (about 1500–3000 m), a V_p/V_s–ϕ_w crossplot was generated to calibrate the empirical V_p/V_s–ϕ_w relationship. In general, such calibration should be performed separately for each sedimentary unit; however, in the present study area, the Jurassic and Paleocene formations exhibit similar relationships, and therefore a single calibration was considered sufficient. Figs. 10(a)–10(f) show the data color-coded by illite, calcite, quartz, oil, gas, and total porosity, respectively, thereby illustrating how various rock-physics attributes are distributed in the ϕ_w–V_p/V_s. The interpretation is based on a three-phase rock-physics model used to differentiate oil-, gas-, and water-bearing facies; the pores in the limestone contain only water. Comparison of Fig. 10(c) and (e) indicates that hydrocarbon-bearing reservoirs in this area are predominantly sandstones (consistent with regional geology) and align along the principal trend; as both ϕ_w and V_p/V_s decrease, the gas response becomes progressively stronger (Fig. 10(e)). Furthermore, Fig. 10(d) and (e) demonstrate

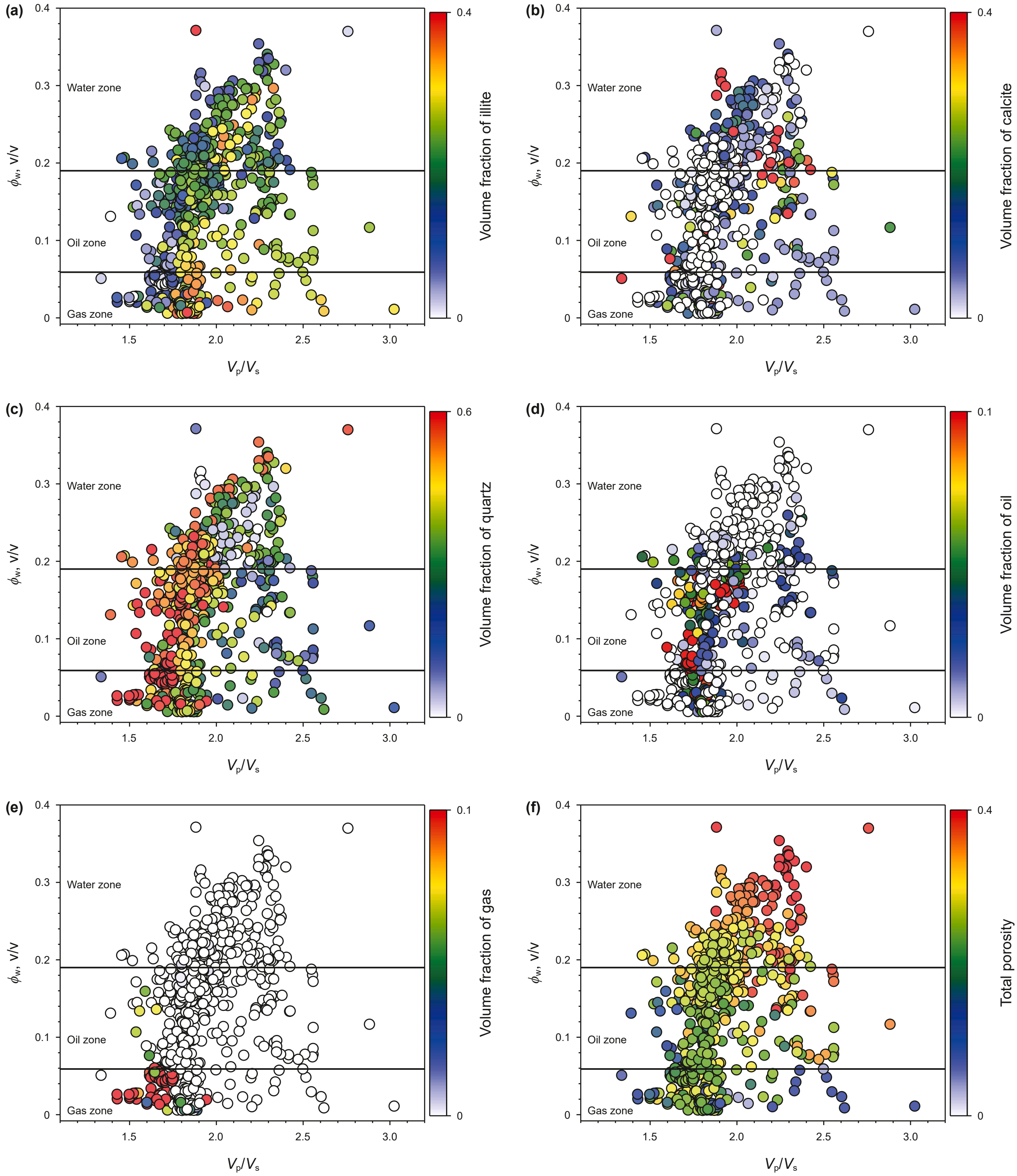

Fig. 10. Crossplots of water-filled porosity (ϕ_w) versus V_p/V_s ratio, color-coded by **(a)** illite volume fraction, **(b)** calcite volume fraction, **(c)** quartz volume fraction, **(d)** oil volume fraction, **(e)** gas volume fraction, and **(f)** total porosity.

that gas, oil, and water facies can be effectively distinguished along both axes, although a certain degree of overlap remains.

Following the identification of the oil, gas, and water zones in the crossplot, several data points are found to correspond to water shales with high V_p/V_s values and to locally calcite-rich limestones. The former typically exhibit $\phi_w < 0.10$, whereas the latter show $\phi_w > 0.14$; neither represents hydrocarbon-bearing formations, and both are excluded from effective hydrocarbon responses. Water carbonates are clearly distinguishable from hydrocarbon-bearing sandstones, preferentially mapping to regions characterized by high V_p/V_s and/or high ϕ_w values (Fig. 10(b)). At any location, the sum of water, oil, and gas volume fractions equals the total porosity (Figs. 10(f) and 11). Fig. 11 presents the crossplot of fluid volume fractions versus water-filled porosity. Hydrocarbon fluids

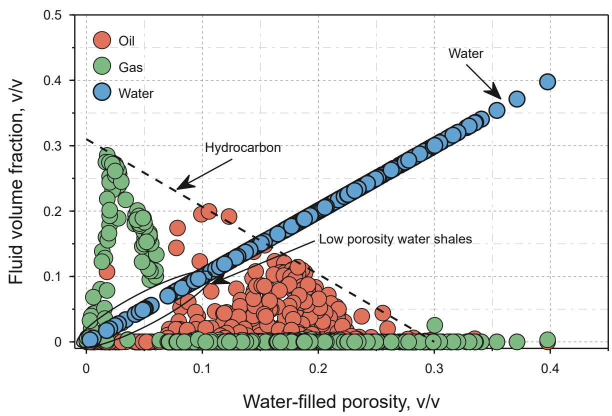

Fig. 11. Crossplot of fluid volume fractions versus water-filled porosity, used for fluid calibration and discrimination of hydrocarbon- and water-dominated facies. Green points denote gas occurrences, red points denote oil occurrences, and blue points denote water occurrences.

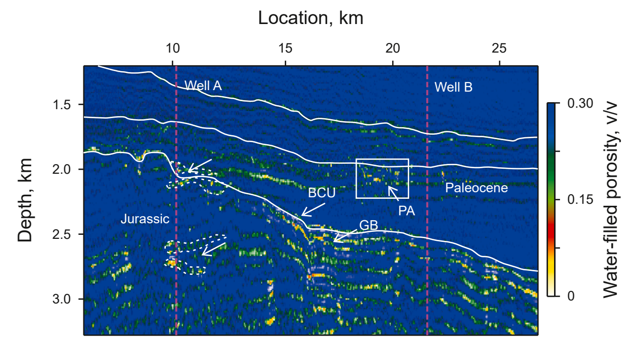

Fig. 13. Estimated water-filled porosity (ϕ_w) section. White dashed lines denote hydrocarbon zones identified from well data.

(oil and gas) are primarily distributed below the hydrocarbon trend line, and their total volumetric fraction decreases progressively with increasing ϕ_w. This systematic distribution provides the basis for fluid calibration, allowing hydrocarbon-bearing intervals to be distinguished from water-dominated lithologies in the crossplot. Notably, the water layers (blue points) located below the hydrocarbon trend line are dominated by low-porosity water shales (Fig. 10(a) and (e)).

Using the empirical relationship (Fig. 12) jointly established from the V_p/V_s–ϕ_w crossplot and the fluid-calibration constraints in Fig. 11, the V_p/V_s section shown in Fig. 9 was converted into a depth-domain ϕ_w section (Fig. 13). Compared with the original V_p/V_s section, the estimated ϕ_w section more intuitively delineates potential hydrocarbon anomalies. Although local overlaps remain, most lithologic and fluid types can be effectively distinguished. Because the empirical relationship was calibrated using well-log data, the low-ϕ_w anomalies observed on the inverted section correlate well with hydrocarbon intervals identified in the wells, providing an indirect validation of the inversion results. In Fig. 13, low ϕ_w values generally indicate potential hydrocarbon zones; however, when $V_p/V_s > 2$ while ϕ_w remains low, these responses represent spurious low-S_w anomalies associated with low-porosity, water shales (Figs. 10(a), 10(f), and 12).

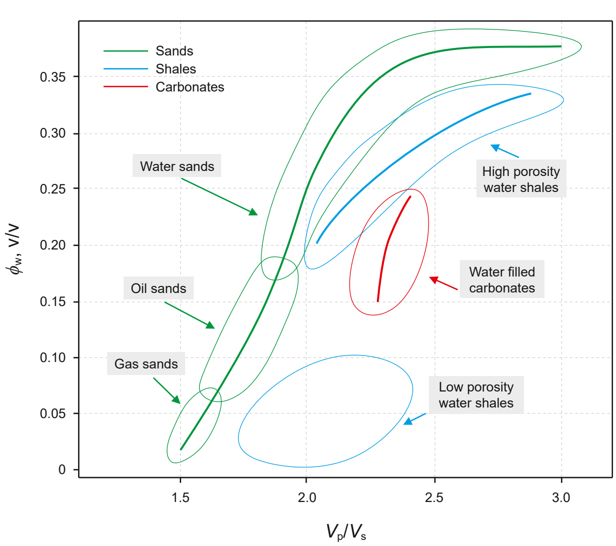

Fig. 12. Fluid-calibrated empirical relationship between V_p/V_s and water-filled porosity (ϕ_w), established from the well-log crossplots in Figs. 10 and 11.

Building on the ϕ_w section, a section geological interpretation was performed. Near Well A, two hydrocarbon-bearing intervals consistent with the well control are identified at approximately 1980–2110 m and 2650–2720 m (Fig. 4). Low-V_p/V_s and low-ϕ_w anomalies occur within the PA. Considering the slope setting, these anomalies are likely associated with turbidites and mass-transport deposits, which create favorable conditions for forming lithologic traps. Therefore, the PA is interpreted as a potential lithologic hydrocarbon reservoir. In the GB zone, the updip flank of the structure is bounded by fault that provides geometric closure. In this rift environment, hydrocarbons migrating updip accumulate against the fault, resulting in an effective fault-bounded trap (Peng et al., 2023).

It should be emphasized that the V_p/V_s–ϕ_w crossplot does not always yield a unique interpretation; however, its primary value lies in its ability to distinguish most hydrocarbon-bearing sandstones from other non-hydrocarbon lithologies and reservoirs (Fig. 10). In this area, the combined conditions of $\phi_w < 0.16$ and $V_p/V_s < 1.8$ can be used as an empirical criterion for identifying potential hydrocarbon-bearing sandstones. These threshold values are broadly consistent with those reported by Madiba and McMechan (2003) for the same dataset, indicating that the inversion results preserve the overall lithology–fluid discrimination trend despite minor numerical differences. A decrease in ϕ_w corresponds to an increasing gas–oil ratio, while a lower V_p/V_s indicates higher sand content and reduced shale content. These threshold values are locally calibrated using well data and should be re-evaluated before being applied to other geological settings or stratigraphic intervals. To mitigate potential bias arising from applying well-log-derived templates to seismic inversion attributes, the crossplot relationships and thresholds are treated as interpretation criteria rather than exact predictors. Prior to template construction, the relevant logs were depth-matched, resampled to a consistent meter-scale vertical sampling, and screened for anomalous values. In addition, the fluid-calibration constraints (Fig. 11) were used to exclude non-hydrocarbon responses (e.g., low-porosity water shales) that could otherwise produce spurious low-ϕ_w anomalies. Consequently, although localized uncertainty may persist in areas with limited illumination or weak well control, the mapped ϕ_w anomalies satisfying the above criteria are broadly consistent with hydrocarbon-bearing intervals observed in the wells, providing a well-tied consistency check for the interpretation. Nevertheless, the proposed workflow is broadly applicable and can be applied to nearby datasets in the same region, provided that the V_p/V_s–ϕ_w relationship is re-calibrated using local well control.

5. Discussion

Under high-frequency asymptotic conditions, an analytical expression for the angle-domain Gaussian-beam PSF was derived, and PP-wave angle-domain PSFs were computed using a Gaussian-beam migration engine to approximate the local Hessian. By leveraging this approximation, the depth-domain simultaneous multi-parameter inversion yields elastic parameters that are stable, high-resolution, and physically consistent, eliminating the need for repeated time–depth conversions (Fletcher et al., 2012; Mao et al., 2022; Duan et al., 2023). Compared with previous applications in which PSFs were utilized primarily for amplitude-preserving imaging or localized parameter estimation, this study extends the use of angle-domain PSFs to reservoir characterization and fluid identification in structurally complex rift basins. The inversion results align well with the regional structural framework and provide quantitative support for reservoir interpretation and well placement.

Despite the demonstrated stability and interpretability of the proposed method, several limitations remain. First, The spatial consistency between the inverted elastic parameters and seismic reflectors primarily arises from their shared physical basis, namely contrasts in elastic impedance (Fig. 8). Such consistency in fact indicates that the inversion correctly captures the fundamental geological factors responsible for generating seismic reflections. However, this correspondence does not imply a simple mapping of seismic amplitudes. By embedding angle-domain PSFs into the inversion, propagation effects are effectively accounted for, allowing the inversion to target the underlying elastic properties of the rocks. Nevertheless, in structurally complex areas with uneven illumination or limited well control, the uncertainty of the inverted results may increase, which can potentially lead to localized discrepancies with the true geological features. Second, reflectivity is currently modeled using the linear Aki–Richards approximation, which is suitable for small to moderate incidence angles but becomes less accurate at larger angles, where higher-order PP terms and mode-conversion effects may be non-negligible. As a result, part of the far-angle information, particularly the components that are more sensitive to shear-related and density-related contrasts, may not be fully exploited. Given the pronounced angle dependence of the angle-domain PSFs and the typical “low–high–low” illumination pattern observed as the incidence angle increases (Fig. 7), excluding large-angle contributions can result in local under-compensation in structurally complex areas. This occurs because PSFs associated with small to moderate angles may not effectively illuminate certain geometrically complex regions, whereas large-angle PSFs can provide complementary illumination to these shadowed zones. If the large-angle PSF information is not incorporated into the inversion process, the accuracy of inversion parameters that are primarily constrained by far-angle information may be degraded. Third, only PP-wave reflections were considered in this study, whereas PS or multicomponent information was not incorporated, limiting sensitivity to certain types of lateral heterogeneity. In addition, although the inverted depth-domain ϕ_{W} section exhibits strong agreement with the well-based rock-physics trends, localized low-ϕ_{W} anomalies may correspond to low-porosity water shales or limestones rather than hydrocarbon zones, indicating the inherent nonuniqueness of the $V_{\mathrm{p}}/V_{\mathrm{s}}$–$\phi_{\mathrm{W}}$ mapping (Fig. 11). Nevertheless, because the framework relies on well-calibrated rock-physics relationships, it remains applicable within the study area and can be extended to other geological settings in the same region, provided that appropriate scale-consistent re-calibration is performed.

Future work will aim to address these limitations. First, large-angle PSF contributions will be explicitly incorporated, and nonlinear update strategies will be adopted to improve both inversion resolution and amplitude fidelity. Second, because PP-wave data alone provide limited sensitivity to shear-related properties and lateral heterogeneity, PSFs for both PP and PS modes will be computed from multicomponent seismic data to enable joint depth-domain inversion and enhance lithology–fluid decoupling. Third, the framework will be extended to three-dimensional datasets and integrated with Bayesian or deep-learning priors to refine the nonlinear mapping from elastic parameters to reservoir properties and quantify associated uncertainties.

6. Conclusion

In this study, we developed an angle-domain PSF–based pre-stack depth-domain inversion method that embeds Gaussian-beam PSFs as local-Hessian approximations within the inversion operator, thereby obviating explicit wavelet estimation and inherently accounting for the effects of complex geological structures on seismic wave propagation. Field application to the Paleocene and Jurassic reservoirs of the Northern Viking Graben demonstrates that the method yields high-resolution and geologically consistent V_{p}, V_{s}, and $V_{\mathrm{p}}/V_{\mathrm{s}}$ sections. By incorporating a well-calibrated $V_{\mathrm{p}}/V_{\mathrm{s}}$–$\phi_{\mathrm{W}}$ relationship into the inverted results, depth-domain fluid identification is achieved, with low-ϕ_{W} anomalies closely corresponding to hydrocarbon-bearing intervals observed in the wells. For the Northern Viking Graben, empirically calibrated thresholds of $\phi_{\mathrm{W}} < 0.16$ and $V_{\mathrm{p}}/V_{\mathrm{s}} < 1.8$ can be used to rapidly screen potential hydrocarbon-bearing sandstone reservoirs. These empirical relationships and thresholds are specific to the study area and reflect local lithological and fluid conditions; therefore, re-calibration using region-specific well-log and rock-physics data is required before applying them to other geological settings. Overall, while the $V_{\mathrm{p}}/V_{\mathrm{s}}$–$\phi_{\mathrm{W}}$ relationship itself is region dependent, the proposed angle-domain PSF–based depth-domain inversion workflow is transferable at the methodological level, providing a robust and efficient approach for quantitative reservoir characterization and fluid prediction in structurally complex rift systems.

CRediT authorship contribution statement

Lei Zhao: Writing – review & editing, Writing – original draft, Data curation. **Wei-Jian Mao:** Supervision, Project administration. **Xue Li:** Visualization.

Declaration of competing interest

The authors declare that they have no known competing financial interests or personal relationships that could have appeared to influence the work reported in this paper.

Acknowledgment

This work is supported by the National Natural Science Foundation of China (No. 42130808 and No. 42204115). Partial data preprocessing and visualization were conducted using the donated Omega2 software, which is gratefully acknowledged. The authors would also like to thank the Editor and the anonymous reviewers for their constructive comments and suggestions, which helped to improve the quality and clarity of this manuscript.

Appendix A. Gaussian-beam Hessian operator

To ensure the generality of the derivation, we begin with the elastic-wave Born forward-modeling framework. Under the weak-scattering assumption, the first-order Born approximation is adopted, in which multicomponent seismic data are generated by applying a linear elastic modeling operator to the scattering potential (Beylkin and Burridge, 1990; Yue et al., 2019; Mao et al., 2022). The corresponding mathematical expressions are formulated as follows:

$$\mathbf{d}(\mathbf{x}_r,\mathbf{x}_s,\omega)=\omega^2\int_\Omega \mathbf{W}(\mathbf{x}_r)\mathbf{G}(\mathbf{x},\mathbf{x}_r,\omega)\mathbf{M}(\mathbf{x})\mathbf{G}(\mathbf{x},\mathbf{x}_s,\omega)F(\omega)\mathrm{d}V(\mathbf{x}), \tag{A.1}$$

where $\mathbf{d}$ $(\mathbf{x}_r, \mathbf{x}_s, \omega)$ denotes the reflected wavefield, and $\mathbf{M}(\mathbf{x})$ denotes the scattering potential. Under the high-frequency approximation, the linearized reflection coefficient $\mathcal{R}$ is proportional to the scattering potential at the specular point, with the proportionality constant determined by the reflection mode and the incidence angle (Shaw and Sen, 2004; Stolt and Weglein, 2012).

$$\mathcal{R}(\mathbf{x},\theta_0)=\frac{i\omega}{2\rho_0\alpha_0\cos\theta_0}\mathbf{M}(\mathbf{x},\theta_0), \tag{A.2}$$

with

$$\mathcal{R}(\mathbf{x},\theta_0)=\mathbf{R}(\theta_0)\ \delta[\widehat{\mathbf{m}}\cdot(\mathbf{x}-\mathbf{x}_r)], \tag{A.3}$$

Here, α_0 and ρ_0 denote the background P-wave velocity and density, respectively; $\widehat{\mathbf{m}}$ is the unit normal to the reflector. We adopt a surface-integral formulation in which the spatial Dirac delta in Eq. (A.3) collapses the volume integral onto the reflector surface, with integration element $\mathrm{d}S(\mathbf{x})$. Because reflector properties vary slowly laterally, we retain this dependence and write the reflection coefficient explicitly as $\mathbf{R}$ $(\mathbf{x}, \theta_0)$ in the forward operator. For converted waves, θ_0 in the scaling is replaced by the S-wave reflection angle θ_s (Snell's law), so that the total scattering angle is $\theta=\theta_0+\theta_s$; for PP reflections, $\theta_0=\theta/2$.

For clarity, in Eqs. (A.2) and (A.3), we define $\mathbf{Q}$ as the scaling factor for the linear relationship between the scattering potential and the reflection coefficient:

$$\mathbf{Q}(\theta_0,\omega)\mathbf{R}(\mathbf{x},\theta_0)=\mathbf{M}(\mathbf{x},\theta_0). \tag{A.4}$$

Substituting Eq. (A.4) into Eq. (A.1) yields

$$\begin{aligned}\mathbf{d}(\mathbf{x}_r,\mathbf{x}_s,\omega)&=\omega^2\int_S \mathrm{d}S(\mathbf{x})F(\omega)\mathbf{W}(\mathbf{x}_r)\mathbf{G}(\mathbf{x},\mathbf{x}_r,\omega)\\&\times\mathbf{Q}(\theta_0,\omega)\mathbf{R}(\mathbf{x},\theta_0)\mathbf{G}(\mathbf{x},\mathbf{x}_s,\omega),\end{aligned} \tag{A.5}$$

where $\mathbf{R}(\mathbf{x},\theta_0)=\left(R^{\mathrm{PP}},R^{\mathrm{S_1P}},R^{\mathrm{S_2P}}\right)^\top$. In this study, pure P-wave sources were assumed. $\mathrm{S_1}$ and $\mathrm{S_2}$ are two independent linearly polarized components of the vector S wave in a 3D ray-centered coordinate system (Červený, 2000; Zhuang et al., 2022). For a fixed angle, the delta function property yields

$$\mathbf{R}(\mathbf{x},\theta_0)=\int \mathrm{d}\theta_t\mathbf{R}(\mathbf{x},\theta_t)\delta(\theta_t-\theta_0), \tag{A.6}$$

where $\mathbf{R}(\mathbf{x},\theta_t)$ denotes the plane-wave reflection coefficients. Combining Eqs. (A.5) and (A.6), the multicomponent reflection data can be approximated as

$$\begin{aligned}\mathbf{d}(\mathbf{x}_r,\mathbf{x}_s,\omega)&=\omega^2\int_S\int \mathrm{d}\theta_t\ \mathrm{d}S(\mathbf{y})F(\omega)\mathbf{W}(\mathbf{x}_r)\mathbf{G}(\mathbf{y},\mathbf{x}_r,\omega)\\&\times\mathbf{G}(\mathbf{y},\mathbf{x}_s,\omega)\mathbf{Q}(\theta_t,\omega)\mathbf{R}_t(\mathbf{y},\theta_t)\delta(\theta_t-\theta_\mathbf{y}),\end{aligned} \tag{A.7}$$

where $\mathbf{y}$ denotes a dummy integration point on the reflector surface, whereas $\mathbf{x}$ is reserved for the image point. The half-scattering angle at $\mathbf{y}$, denoted by $\theta_\mathbf{y}=\theta_\mathbf{y}(\mathbf{x}_r,\mathbf{y},\mathbf{x}_s)$, is defined locally at the scatterer, and the subscript emphasizes its spatial dependence. Importantly, a physically valid reflectivity $\mathbf{R}_t(\mathbf{y}, \theta_t)$ exists for all admissible angles at $\mathbf{y}$, irrespective of whether any specific source–receiver pair illuminates that configuration. In other words, θ_t is governed by the intrinsic scattering properties of the subsurface rather than by the acquisition geometry. Applying the adjoint operator $\mathbf{L}^\top$ of $\mathbf{L}$ to the recorded data $\mathbf{d}$ produces the migrated seismic image:

$$\begin{aligned}\mathbf{R}_{\mathrm{mig}}(\mathbf{x},\theta)&=\mathbf{L}^\top\mathbf{d}\\&=\iint \mathrm{d}\mathbf{x}_r\mathrm{d}\mathbf{x}_s\int \mathrm{d}\omega\ \omega^2F(\omega)\ \delta(\theta-\theta_\mathbf{x})\mathbf{Q}^\top(\theta_\mathbf{x},\omega)\\&\times\mathbf{G}^*(\mathbf{x},\mathbf{x}_r,\omega)\mathbf{W}^\top(\mathbf{x}_r)\mathbf{d}(\mathbf{x}_r,\mathbf{x}_s,\omega)\mathbf{G}^*(\mathbf{x},\mathbf{x}_s,\omega).\end{aligned} \tag{A.8}$$

To highlight the dependence of the half-scattering angle on spatial coordinates, we define $\theta_\mathbf{x}=\theta_0(\mathbf{x}_r,\mathbf{x},\mathbf{x}_s)$ within the migration operator. Substituting the multicomponent data $\mathbf{d}$ into Eq. (A.8) and reorganizing the terms yields

$$\mathbf{R}_{\mathrm{mig}}(\mathbf{x},\theta)=\int \mathrm{d}\mathbf{y}\int \mathrm{d}\theta_t\mathbf{H}(\mathbf{x},\theta;\mathbf{y},\theta_t)\mathbf{R}_t(\mathbf{y},\theta_t), \tag{A.9}$$

which is Eq. (1) in the main text.

Accordingly, the migrated image $\mathbf{R}_{\mathrm{mig}}(\mathbf{x}, \theta)$ can be regarded as the true angle-dependent reflectivity $\mathbf{R}_t(\mathbf{y}, \theta_t)$ after filtering by the kernel $\mathbf{H}$ $(\mathbf{x}, \theta; \mathbf{y}, \theta_t)$. In operator form, $\mathbf{R}_{\mathrm{mig}}=\mathbf{H}\mathbf{R}_t=\mathbf{L}^\top\mathbf{L}\mathbf{R}_t$. The kernel $\mathbf{H}$ $(\mathbf{x}, \theta; \mathbf{y}, \theta_t)$ is given by

$$\begin{aligned}\mathbf{H}(\mathbf{x},\theta;\mathbf{y},\theta_t)&=\iint \mathrm{d}\mathbf{x}_r\mathrm{d}\mathbf{x}_s\int \mathrm{d}\omega\ \omega^4|F(\omega)|^2\delta(\theta-\theta_\mathbf{x})\delta(\theta_t-\theta_\mathbf{y})\\&\times\mathbf{W}^\top(\mathbf{x}_r)\mathbf{G}^*(\mathbf{x},\mathbf{x}_r,\omega)\mathbf{G}^*(\mathbf{x},\mathbf{x}_s,\omega)\mathbf{Q}^\top(\theta_\mathbf{x},\omega)\\&\times\mathbf{W}(\mathbf{x}_r)\mathbf{G}(\mathbf{y},\mathbf{x}_r,\omega)\mathbf{G}(\mathbf{y},\mathbf{x}_s,\omega)\mathbf{Q}(\theta_\mathbf{y},\omega),\end{aligned} \tag{A.10}$$

where $|\cdot|$ denotes the complex signal modulus. Table A.2 reviews the physical meanings of different angle variables in Eq. (A.10).

Table A.2
The physical meanings of different angle variables in Eq. (A.10)

Angle	Description
$\theta_\mathbf{x}(\mathbf{x}_r, \mathbf{x}, \mathbf{x}_s)$	Half-scattering angle at the image point $\mathbf{x}$.
$\theta_\mathbf{y}(\mathbf{x}_r, \mathbf{y}, \mathbf{x}_s)$	Half-scattering angle evaluated at the actual reflector point $\mathbf{y}$.
θ_t	The reflection angle index of angle-dependent reflection coefficient $\mathbf{R}_t(\mathbf{y}, \theta_t)$.
θ	The reflection angle index of ADCIGs $\mathbf{R}_{\mathrm{mig}}(\mathbf{x}, \theta)$.

Green's function for the upgoing wave can be expressed as the sum of the elastic Gaussian beams (Červený, 2000; Gray and Bleistein, 2009; Li and Mao, 2016; Yue et al., 2019; Mao et al., 2022):

$$G(\mathbf{x}|\mathbf{x}_s;\omega) = \frac{i\omega}{2\pi}\iint\frac{\mathrm{d}p_x\mathrm{d}p_y}{p_z^w}\mathbf{u}_{\mathrm{GB}}(\mathbf{x}|\mathbf{x}_s;\mathbf{p},\omega), \tag{A.11}$$

where $\mathbf{u}_{\mathrm{GB}}(\mathbf{x}|\mathbf{x}_s;\,\mathbf{p},\,\omega)$ represents the Gaussian beam generated at the source location $\mathbf{x}_s$ for the upgoing wave. Here, $\mathbf{p} = (p_x, p_y, p_z)^\top$ denotes the initial ray parameter vector of the central ray on the surface. Li and Mao (2016) presented a unified multimode formulation for Gaussian beams. Substituting Eq. (A.11) for the source and receiver Green's functions into Eq. (A.10) yields the explicit Gaussian-beam Hessian (Zhang et al., 2024b; Mao et al., 2022):

$$\begin{aligned}\mathbf{H}(\mathbf{x},\theta;\mathbf{y},\theta_t) &= \iint\mathrm{d}\mathbf{x}_r\mathrm{d}\mathbf{x}_s\int\mathrm{d}\omega\frac{\omega^8}{(2\pi)^4}|F(\omega)|^2\delta(\theta-\theta_\mathbf{x})\delta(\theta_t-\theta_\mathbf{y})\\ &\times\mathbf{W}^\top(\mathbf{x}_r)\iint\frac{\mathrm{d}p_x\mathrm{d}p_y}{p_z^w}\mathbf{u}_{\mathrm{GB}}^{w*}(\mathbf{x}|\mathbf{x}_r;\mathbf{p}^w,\omega)\\ &\times\mathbf{W}(\mathbf{x}_r)\iint\frac{\mathrm{d}p_x\mathrm{d}p_y}{p_z^v}\mathbf{u}_{\mathrm{GB}}^{v*}(\mathbf{x}|\mathbf{x}_s;\mathbf{p}^v,\omega)\\ &\times\mathbf{Q}^\top(\theta_\mathbf{x},\omega)\iint\frac{\mathrm{d}p_x\mathrm{d}p_y}{p_z^w}\mathbf{u}_{\mathrm{GB}}^{w}(\mathbf{y}|\mathbf{x}_r;\mathbf{p}^w,\omega)\\ &\times\mathbf{Q}(\theta_\mathbf{y},\omega)\iint\frac{\mathrm{d}p_x\mathrm{d}p_y}{p_z^v}\mathbf{u}_{\mathrm{GB}}^{v}(\mathbf{y}|\mathbf{x}_s;\mathbf{p}^v,\omega),\end{aligned} \tag{A.12}$$

where the superscripts v and w denote the downgoing v-model of the source side and the upgoing w-mode wave of the receiver side, respectively.

Appendix B. High-frequency asymptotic Gaussian-beam PSFs

Starting with the existing Gaussian-beam Hessian operator, we obtain

$$\mathbf{H}(\mathbf{x},\theta;\mathbf{y},\theta_t) = \iint\mathrm{d}\mathbf{x}_r\mathrm{d}\mathbf{x}_s\delta(\theta_t-\theta_\mathbf{y})\mathbf{K}_{\mathrm{GB}}(\mathbf{x},\theta,\mathbf{y},\mathbf{x}_r,\mathbf{x}_s) \tag{B.1}$$

with

$$\begin{aligned}\mathbf{K}_{\mathrm{GB}}(\mathbf{x},\theta,\mathbf{y},\mathbf{x}_r,\mathbf{x}_s) &= \int\mathrm{d}\omega\frac{\omega^8}{(2\pi)^4}|F(\omega)|^2\delta(\theta-\theta_\mathbf{x})\\ &\times\mathbf{W}^\top(\mathbf{x}_r)\iint\frac{\mathrm{d}p_x\mathrm{d}p_y}{p_z^w}\mathbf{u}_{\mathrm{GB}}^{w*}(\mathbf{x}|\mathbf{x}_r;\mathbf{p}^w,\omega)\\ &\times\mathbf{W}(\mathbf{x}_r)\iint\frac{\mathrm{d}p_x\mathrm{d}p_y}{p_z^v}\mathbf{u}_{\mathrm{GB}}^{v*}(\mathbf{x}|\mathbf{x}_s;\mathbf{p}^v,\omega)\\ &\times\mathbf{Q}^\top(\theta_\mathbf{x},\omega)\iint\frac{\mathrm{d}p_x\mathrm{d}p_y}{p_z^w}\mathbf{u}_{\mathrm{GB}}^{w}(\mathbf{y}|\mathbf{x}_r;\mathbf{p}^w,\omega)\\ &\times\mathbf{Q}(\theta_\mathbf{y},\omega)\iint\frac{\mathrm{d}p_x\mathrm{d}p_y}{p_z^v}\mathbf{u}_{\mathrm{GB}}^{v}(\mathbf{y}|\mathbf{x}_s;\mathbf{p}^v,\omega).\end{aligned} \tag{B.2}$$

Substituting Eq. (B.1) into Eq. (A.9) and integrating with respect to θ_t yields

$$\mathbf{R}_{\mathrm{mig}}(\mathbf{x},\theta) = \int\mathrm{d}\mathbf{y}\iint\mathrm{d}\mathbf{x}_r\mathrm{d}\mathbf{x}_s\mathbf{K}_{\mathrm{GB}}(\mathbf{x},\theta,\mathbf{y},\mathbf{x}_r,\mathbf{x}_s)\mathbf{R}_t(\mathbf{y},\theta_\mathbf{y}). \tag{B.3}$$

In the integral $\int d\mathbf{y}\iint \mathrm{d}\mathbf{x}_r\mathrm{d}\mathbf{x}_s$, substituting the true plane-wave reflectivity $\mathbf{R}_t(\mathbf{y},\theta_\mathbf{y}(\mathbf{x}_r,\mathbf{y},\mathbf{x}_s) = \mathbf{R}_t(\mathbf{y},\theta)$ reduces Eq. (B.3) to

$$\mathbf{R}_{\mathrm{mig}}(\mathbf{x},\theta) = \int\mathrm{d}\mathbf{y}\;\mathbf{PSF}(\mathbf{x},\theta;\mathbf{y})\mathbf{R}_t(\mathbf{y},\theta). \tag{B.4}$$

which is Eq. (2) in the main text, $\mathbf{PSF}(\mathbf{x},\,\theta;\,\mathbf{y})$ is expressed as

$$\mathbf{PSF}(\mathbf{x},\theta;\mathbf{y}) = \iint d\mathbf{x}_r d\mathbf{x}_s\mathbf{K}_{\mathrm{GB}}(\mathbf{x},\theta,\mathbf{y};\mathbf{x}_r,\mathbf{x}_s), \tag{B.5}$$

which is Eq. (3) in the main text. In the above derivation, the half-scattering angle $\theta_\mathbf{y}(\mathbf{x}_r,\mathbf{y},\mathbf{x}_s)$ is replaced by the discrete angle index θ used in constructing the ADCIGs. Such a substitution is valid only under the high-frequency asymptotic assumption. Within this limit, each individual source–receiver pair contributes to the migrated image exclusively at the local specular angle $\theta = \theta_\mathbf{y}$. Accordingly, all rays falling within a narrow angular interval are considered to sample an identical plane-wave reflection coefficient, allowing the complete data-space integral to be reduced to its angle-domain PSF representation. For band-limited data, the specular response is no longer an exact delta function in angle. Even so, the high-frequency approximation remains sufficiently accurate for the angular sampling typically used in ADCIG construction and constitutes the theoretical foundation of most practical image-domain inversion (Zhang et al., 2024b).

References

Aki, K., Richards, P.G., 1980. Quantitative Seismology: Theory and Methods. W. H. Freeman and Company, San Francisco.

An, Z., Wen, X., Sun, S., et al., 2025. Time–frequency mixed–domain impedance inversion for nonstationary seismic based on frequency-dependent Q. IEEE Trans. Geosci. Rem. Sens. 63, 1–16. https://doi.org/10.1109/TGRS.2025.3581059.

Bai, J., Yilmaz, O., 2022. Image-domain angle/azimuth-dependent least-squares reverse-time migration through point spread functions. In: Proceedings of the 83rd EAGE Annual Conference and Exhibition. https://doi.org/10.3997/2214-4609.202210306.

Beylkin, G., Burridge, R., 1990. Linearized inverse scattering problems in acoustics and elasticity. Wave Motion 12 (1), 15–52. https://doi.org/10.1016/0165-2125(90)90017-X.

Buland, A., Omre, H., 2003. Bayesian linearized AVO inversion. Geophysics 68 (1), 185–198. https://doi.org/10.1190/1.1543206.

Cavalca, M., Fletcher, R.P., 2023. PP-PS depth-domain AVA inversion. In: SEG Technical Program Expanded Abstracts, pp. 74–78. https://doi.org/10.1190/image2023-3911550.1.

Červený, V., 2000. Seismic Ray Method. Cambridge University Press.

Dai, W., Xu, Z., Cheng, X., et al., 2019. Image-domain least-squares migration for RTM surface-offset gathers. In: Proceedings of the 81st EAGE Conference and Exhibition, pp. 1–5. https://doi.org/10.3997/2214-4609.201900827.

Duan, W., Mao, W., Shi, X., et al., 2023. Iterative reweighted least-squares Gaussian beam migration and velocity inversion in the image domain based on point spread functions. IEEE Trans. Geosci. Rem. Sens. 61, 1–12. https://doi.org/10.1109/TGRS.2023.3274212.

Fletcher, R.P., Archer, S., Nichols, D., et al., 2012. Inversion after depth imaging. In: SEG Technical Program Expanded, pp. 1–5. https://doi.org/10.1190/segam2012-0427.1.

Fletcher, R.P., Nichols, D., Bloor, R., et al., 2016. Least-squares migration—data domain versus image domain using point spread functions. Lead. Edge 35 (2), 157–162. https://doi.org/10.1190/tle35020157.1.

Gautier, D.L., 2005. Kimmeridgian Shales Total Petroleum System of the North Sea Graben Province. U.S. Geological Survey.

Gelius, L., Lecomte, I., Tabti, H., 2002. Analysis of the resolution function in seismic prestack depth imaging. Geophys. Prospect. 50 (5), 505–515. https://doi.org/10.1046/j.1365-2478.2002.00331.x.

Grana, D., 2016. Bayesian linearized rock-physics inversion. Geophysics 81 (6), D625–D641. https://doi.org/10.1190/geo2016-0161.1.

Gray, S.H., Bleistein, N., 2009. True-amplitude Gaussian-beam migration. Geophysics 74 (2), S11–S23. https://doi.org/10.1190/1.3052116.

Hill, N.R., 2001. Prestack Gaussian-beam depth migration. Geophysics 66, 1240–1250. https://doi.org/10.1190/1.1487071.

Hilterman, F., 1990. Is AVO the seismic signature of lithology? A case history of Ship Shoal-South addition. Lead. Edge 9 (6), 15–22. https://doi.org/10.1190/1.1439744.
Jensen, K., Lecomte, I., Gelius, L.J., et al., 2021. Point-spread function convolution to simulate prestack depth migrated images: A validation study. Geophys. Prospect. 69 (8–9), 1571–1590. https://doi.org/10.1111/1365-2478.13132.
Jiang, B., Zhang, J., Zhang, H., et al., 2022. Fast least-squares prestack time migration via accelerating the explicit calculation of Hessian matrix with dip-angle fresnel zone. Pet. Sci. 19 (3), 1031–1047. https://doi.org/10.1016/j.petsci.2021.12.017.
Kumar, D., 2023. Chapter nine – seismic AVO analysis for reservoir characterization. In: Reservoir Characterization, Modeling, and Quantitative Interpretation, vol. 6. Elsevier, pp. 259–284. https://doi.org/10.1016/B978-0-323-99593-1.00002-1.
Lang, X., Grana, D., 2017. Geostatistical inversion of prestack seismic data for the joint estimation of facies and impedances using stochastic sampling from Gaussian mixture posterior distributions. Geophysics 82 (4), M55–M65. https://doi.org/10.1190/geo2016-0670.1.
Lecomte, I., 2008. Resolution and illumination analyses in PSDM: A ray-based approach. Lead. Edge 27 (5), 650–663. https://doi.org/10.1190/1.2919584.
Lecomte, I., Lavadera, P.L., Anell, I., et al., 2015. Ray-based seismic modeling of geologic models: Understanding and analyzing seismic images efficiently. Interpretation 3 (4), SAC71–SAC89. https://doi.org/10.1190/INT-2015-0061.1.
Lee, M.W., Collett, T.S., 2001. Elastic properties of gas hydrate-bearing sediments. Geophysics 66 (3), 763–771. https://doi.org/10.1190/1.1444966.
Letki, L., Tang, J., Inyang, C., et al., 2015. Depth domain inversion to improve the fidelity of subsalt imaging: A Gulf of Mexico case study. First Break 33 (9). https://doi.org/10.3997/1365-2397.33.9.82617.
Levin, A., Fergus, R., Durand, F., et al., 2007. Deconvolution using natural image priors. ACM Trans. Graph. 26.
Li, X., Mao, W., 2016. Multimode and multicomponent Gaussian beam prestack depth migration. Chin. J. Geophys. 59 (8), 2989–3005. https://doi.org/10.6038/cjg20160822 (in Chinese).
Madiba, G.B., McMechan, G.A., 2003. Processing, inversion, and interpretation of a 2D seismic data set from the North Viking Graben, North Sea. Geophysics 68 (3), 837–848. https://doi.org/10.1190/1.1581036.
Mao, W., Duan, W., Sun, C., et al., 2022. Elastic least-squares Gaussian beam imaging with point spread functions. IEEE Geosci. Rem. Sens. Lett. 19, 1–5. https://doi.org/10.1109/LGRS.2022.3173303.
Olutoki, J.O., guo Zhao, J., Siddiqui, N.A., et al., 2024. Shear wave velocity prediction: A review of recent progress and future opportunities. Energy Geosci. 5 (4), 100338. https://doi.org/10.1016/j.engeos.2024.100338.
Osorio, L.N., Pereira-Dias, B., Bulcão, A., et al., 2021. Migration deconvolution using domain decomposition. Geophysics 86 (3), S247–S256. https://doi.org/10.1190/geo2020-0352.1.
Ostrander, W.J., 1984. Plane-wave reflection coefficients for gas sands at non-normal angles of incidence. Geophysics 49 (10), 1637–1648. https://doi.org/10.1190/1.1441571.
Peng, G., Wu, Z., Dai, Y., et al., 2023. Quantitative evaluation and models of hydrocarbon accumulation controlled by faults in the Pearl River mouth basin. Adv. Geo-Energy Res. 8 (2), 89–99. https://doi.org/10.46690/ager.2023.05.03.
Qin, X., Zhao, L., Cai, Z., et al., 2022. Compressional and shear wave velocities relationship in anisotropic organic shales. J. Pet. Sci. Eng. 219, 111070. https://doi.org/10.1016/j.petrol.2022.111070.
Schuster, G.T., Hu, J., 2000. Green's function for migration: continuous recording geometry. Geophysics 65 (1), 167–175. https://doi.org/10.1190/1.1444707.
Sengupta, M., Zhang, H., Zhao, Y., et al., 2021. Direct depth-domain Bayesian amplitude-variation-with-offset inversion. Geophysics 86 (5), M167–M176. https://doi.org/10.1190/geo2020-0219.1.
Shaw, R.K., Sen, M.K., 2004. Born integral, stationary phase and linearized reflection coefficients in weak anisotropic media. Geophys. J. Int. 158 (1), 225–238. https://doi.org/10.1111/j.1365-246X.2004.02283.x.
Sherwood, J.W., Sherwood, K., Tieman, H., et al., 2009. 3D beam prestack depth migration with examples from around the world. Lead. Edge 28 (9), 1120–1127. https://doi.org/10.1190/1.3236382.
Shi, X., Ouyang, W., Mao, W., 2023. True-amplitude Gaussian-beam migration for acoustic transversely isotropic media with a vertical symmetry axis. IEEE Trans. Geosci. Rem. Sens. 61, 1–10. https://doi.org/10.1109/TGRS.2023.3310207.
Singh, Y., 2012. Deterministic inversion of seismic data in the depth domain. Lead. Edge 31 (5), 538–545. https://doi.org/10.1190/geo2020-0219.1.
Stolt, R.H., Weglein, A.B., 2012. Seismic Imaging and Inversion: Application of Linear Inverse Theory. Cambridge University Press.
Surlyk, F., Dons, T., Clausen, C.K., et al., 2003. Upper cretaceous. In: Evans, D., Graham, C., Armour, A., et al. (Eds.), The Millennium Atlas: Petroleum Geology of the Central and Northern North Sea. Geological Society of London, London, pp. 213–233.
Turner, C.C., Cronin, B.T., Riley, L.A., et al., 2018. The South Viking Graben: Overview of Upper Jurassic Rift Geometry, Biostratigraphy, and Extent of Brae Play Submarine Fan Systems, In: Rift-Related Coarse-Grained Submarine Fan Reservoirs; the Brae Play, South Viking Graben, North Sea. the American Association of Petroleum Geologists, 115. AAPG Memoir. https://doi.org/10.1306/13652177M1153807.
Underhill, J.R., Richardson, N., 2022. Geological controls on petroleum plays and future opportunities in the north sea rift super basin. AAPG Bull. 106 (3), 573–631. https://doi.org/10.1306/07132120084.
Valenciano, A., Orlovich, M., Klochikhina, E., et al., 2019. Least-squares wave equation migration with angle gathers. In: Proceedings of the 81st EAGE Conference and Exhibition, pp. 1–5. https://doi.org/10.3997/2214-4609.201900824.
Wang, J.Q., Deng, J.X., Xu, Z.H., et al., 2024. Rock physics properties and influencing factors of subsalt carbonate reservoir of ordovician majiagou formation in central ordos basin. Pet. Sci. 21 (6), 3965–3980. https://doi.org/10.1016/j.petsci.2024.05.024.
Wang, Y.R., Zong, Z.Y., Yin, X.Y., 2022. Fluid discrimination incorporating amplitude variation with angle inversion and squirt flow of the fluid. Pet. Sci. 19 (4), 1592–1604. https://doi.org/10.1016/j.petsci.2022.03.007.
Wei, F., Tian-Yue, H., Feng-Chang, Y., et al., 2017. Time-varying seismic wavelet estimation from nonstationary seismic data. Chin. J. Geophys. 60 (2), 191–202. https://doi.org/10.1002/cjg2.30038.
Wu, C., Han, L., Zhang, F., et al., 2023. Gas hydrate reservoir identification based on rock physics modelling and sensitive elastic parameters. J. Geophys. Eng. 20 (1), 117–127. https://doi.org/10.1093/jge/gxac100.
Yang, J., Huang, J., Zhu, H., et al., 2022. An efficient and stable high-resolution seismic imaging method: point-spread function deconvolution. J. Geophys. Res. Solid Earth 127 (7). https://doi.org/10.1029/2021JB023281 e2021JB023281.
Yuan, H., hua Han, D., Wang, Y., 2022. A review of rock physical models for elastic properties characterization of gas hydrate bearing sediments. J. Pet. Sci. Eng. 218, 111013. https://doi.org/10.1016/j.petrol.2022.111013.
Yue, Y., Liu, Y., Li, Y., et al., 2021. Least-squares Gaussian beam migration in viscoacoustic media. Geophysics 86 (1), S17–S28. https://doi.org/10.1190/geo2020-0129.1.
Yue, Y., Sava, P., Qian, Z., et al., 2019. Least-squares Gaussian beam migration in elastic media. Geophysics 84 (4), S329–S340. https://doi.org/10.1190/geo2018-0391.1.
Zachariah, A.J., Gawthorpe, R., Dreyer, T., 2009. Evolution and strike variability of early post-rift deep-marine depositional systems: lower to mid-cretaceous, North Viking Graben, Norwegian North Sea. Sediment. Geol. 220 (1), 60–76. https://doi.org/10.1016/j.sedgeo.2009.06.006.
Zhang, R., Deng, Z., 2023. Depth-domain angle and depth variant seismic wavelets extraction for prestack seismic inversion. Geophysics 88 (1), R1–R10. https://doi.org/10.1190/geo2021-0647.1.
Zhang, R., Fomel, S., 2017. Time-variant wavelet extraction with a local-attribute-based time-frequency decomposition for seismic inversion. Interpretation 5 (1), SC9–SC16. https://doi.org/10.1190/INT-2016-0060.1.
Zhang, W., Gao, J., Shi, Y., et al., 2024a. Q-compensated image-domain least-squares reverse time migration through preconditioned point-spread functions. Geophysics 89 (3), S195–S213. https://doi.org/10.1190/geo2023-0333.1.
Zhang, W., Guo, X., Ravasi, M., et al., 2024b. Angle-dependent image-domain least-squares migration through analytical point spread functions. Geophysics 89 (5), S339–S360. https://doi.org/10.1190/geo2023-0499.1.
Zhao, L., Mao, W., Liu, Z., et al., 2023. Research on the differential tectonic-thermal evolution of longmaxi shale in the southern sichuan basin. Adv. Geo-Energy Res. 7 (3), 152–163. https://doi.org/10.46690/ager.2023.03.02.
Zhou, L., Liao, J.P., Liu, X.Y., et al., 2023. A high resolution inversion method for fluid factor with dynamic dry-rock vp/vs ratio squared. Pet. Sci. 20 (5), 2822–2834. https://doi.org/10.1016/j.petsci.2023.09.015.
Zhuang, S., Huang, J., Yang, J., et al., 2022. A computational method for wide-azimuth 3D dip-angle gathers using Gaussian beam migration. Pet. Sci. 19 (5), 2081–2094. https://doi.org/10.1016/j.petsci.2022.03.012.
Zong, Z., Feng, Y., Yin, X., et al., 2021. Fluid discrimination incorporating visco-elasticity and frequency-dependent amplitude variation with offsets inversion. Pet. Sci. 18 (4), 1047–1058. https://doi.org/10.1016/j.petsci.2020.10.001.
Zuo, Y., Zong, Z., Yin, X., et al., 2025. Bayesian AVO inversion of fluid and anisotropy parameters in VTI media using IADR-Gibbs algorithm. Pet. Sci. 22 (9), 3565–3582. https://doi.org/10.1016/j.petsci.2025.05.006.